Int. J. Heat Mass Transfer. Vol. 35, No. 4, pp. 803–814, 1992
Printed in Great Britain

0017–9310/92 $5.00 + 0.00
Pergamon Press plc

Heat transfer in a channel with built-in wing-type vortex generators

G. BISWAS† and H. CHATTOPADHYAY‡

Department of Mechanical Engineering, Indian Institute of Technology, Kharagpur (W.B.) 721302, India

(*Received* 15 *January* 1990 *and in final form* 11 *January* 1991)

Abstract—An extension of earlier work is made in the present paper to determine numerically the structure of flow and heat transfer characteristics in a rectangular channel with a built-in delta wing protruding from the bottom wall. The predictions are made through the numerical solution of complete Navier–Stokes and energy equations. Augmentation of heat transfer between the flowing fluid and channel wall is seen. The effect of a punched hole, beneath the wing-type vortex generator, on the heat transfer and skin friction characteristics has been determined. The influence of the vortex generator's angle of attack and Reynolds number on heat transfer and skin friction is determined. The combined spanwise average Nusselt number showed increases as large as 34% even at the exit of a long channel at an angle of attack of 26°.

INTRODUCTION

LONGITUDINAL vortices embedded in shear flows occur in many flow situations and may have a remarkable influence on design and development of various kinds of heat exchangers. Figures 1(a) and (b) show typical arrangements of two different heat exchanger cores. In most practical cases, the heat transfer coefficients on the flat surfaces are significantly low. In order to increase heat transfer between the gas and the fin in the case of gas–liquid fin-tube cross-flow heat exchangers and between the flowing fluid and plates in the case of plate-fin heat exchangers, protrusions can be mounted on the flat surfaces. The protrusions, in the form of wing-type vortex generators (Fig. 2) with an angle of attack, can bring about the desired augmentation in heat transfer at the expense of relatively less increase in pressure drop. These wing-type vortex generators will induce longitudinal vortices behind them which will take the fluid from the underside of the wake and swirl it around to the upper side, entraining fluid from the periphery to the centre of the vortices. This mechanism will finally culminate in the disruption of the growth of the thermal boundary layer and the heat transfer coefficient will be enhanced. Also, these slender wings can act as spacers for the plates. Typically, the Reynolds numbers for such applications lie below 3000. Eibeck and Eaton [1] have mentioned that in the presence of favourable pressure gradients the longitudinal vortices will be stable and their influence should persist in an area which is many times larger than the wing area. A number of experimental works [2–4] in fields relevant to the present problem have been reported in literature. Numerical investigations in related areas have been reported earlier by Biswas *et al.* [5, 6]. In their work [6], the combined effect of wing-type vortex generators and mixed convection conditions on heat transfer enhancement is studied. It is found that mixed convection conditions give rise to counter-rotating vortices of the same orientation as the delta wing and heat transfer is improved still further. However, in practice the wings can easily be manufactured by punching or embossing the channel wall. In the earlier

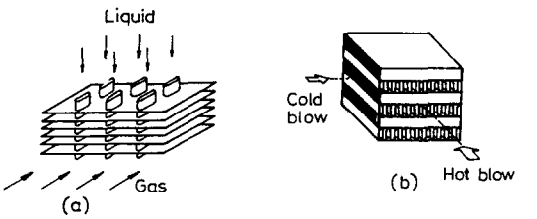

FIG. 1. Typical arrangement of heat exchanger cores. (a) Gas–liquid fin-tube cross-flow. (b) Plate-fin (single or multi pass).

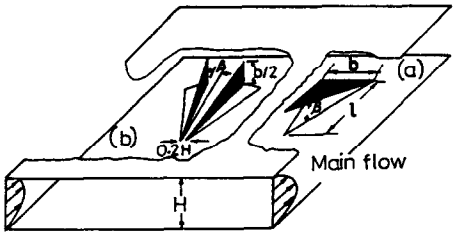

FIG. 2. Protrusions in the form of delta wing (a) and winglet pair (b) on the flat surface to enhance heat transfer.

† Present address: Department of Mechanical Engineering, Indian Institute of Technology, Kanpur (U.P.) 208016, India.

‡ Present address: Central Mechanical Engineering Research Institute, Durgapur (W.B.) 713209, India.

NOMENCLATURE

B	channel width
Br	ratio of wing span to width of the channel, b/B
b	wing span
C_p	specific heat of the fluid
D	divergence of velocity vectors, equation (1)
f_x	skin fraction, $2-(\partial u/\partial y)_w/\rho U_{av}^2$
$\bar{f}$	combined spanwise average friction factor, equation (7)
H	channel height
h	heat transfer coefficient, $-k(\partial T/\partial y)_w/(T_w-T_b)$
k	thermal conductivity of the fluid
Nu	local Nusselt number based on bulk temperature of the fluid, hH/k
Nu_{xe}	local Nusselt number based on entry temperature of the fluid, equation (8)
$\overline{Nu}$	spanwise average Nusselt number
n	iterations in time step
P	nondimensional pressure, $p/\rho U_{av}^2$
Pr	Prandtl number, $\mu C_p/k$
p	pressure
q	wall heat flux
Re	Reynolds number, $U_{av}H/v$
S	wing area
T	temperature
t	time
U	u/U_{av}
u	axial component of velocity
V	v/U_{av}
v	vertical component of velocity
W	w/U_{av}
w	spanwise component of velocity
X	x/H
x	axial dimension of the coordinates
Y	y/H
y	vertical or normal dimension of coordinates
Z	z/H
z	spanwise dimension of coordinates.

Greek symbols

α	aspect ratio of the channel, B/H
Λ	aspect ratio of the wing, b^2/S
μ	dynamic viscosity of the fluid
v	kinematic viscosity of the fluid
τ	nondimensional time.

Subscripts

av	average
b	bulk condition
sa	spanwise combination of top and bottom plates
w	wall
1	bottom fin-plate
2	top fin-plate.

work [6], the effects due to the hole beneath the wing generator was not taken into account. In addition, the influence of angle of attack and Reynolds number on heat transfer and skin friction coefficients were not obtained. Therefore, in the present paper, an extension of the earlier work [6] is made to envisage the objectives enumerated above.

STATEMENT OF THE PROBLEM

Computation is performed in a channel which is formed by two neighbouring fins (Fig. 3). For detailed investigations, only one delta wing (of zero thickness) is placed inside it. The base of the wing is fixed at the bottom wall and the apex faces the incoming stream with an angle of attack. Since symmetry prevails in the vertical central plane of the channel, the flow field in only half of the channel has to be computed. The dimensionless equations for continuity, momentum and energy may be expressed in the following conservative form as

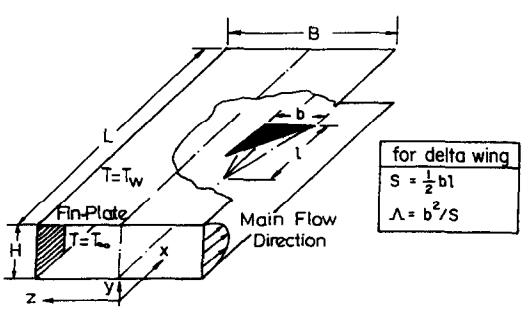

FIG. 3. Flow model for computation.

$$D=\frac{\partial U}{\partial X}+\frac{\partial V}{\partial Y}+\frac{\partial W}{\partial Z}=0 \tag{1}$$

$$\frac{\partial U}{\partial \tau}+\frac{\partial U^2}{\partial X}+\frac{\partial UV}{\partial Y}+\frac{\partial UW}{\partial Z}=-\frac{\partial P}{\partial X}+\frac{\nabla^2 U}{Re} \tag{2}$$

$$\frac{\partial V}{\partial \tau}+\frac{\partial UV}{\partial X}+\frac{\partial V^2}{\partial Y}+\frac{\partial VW}{\partial Z}=-\frac{\partial P}{\partial Y}+\frac{\nabla^2 V}{Re} \tag{3}$$

$$\frac{\partial W}{\partial \tau}+\frac{\partial UW}{\partial X}+\frac{\partial VW}{\partial Y}+\frac{\partial W^2}{\partial Z}=-\frac{\partial P}{\partial Z}+\frac{\nabla^2 W}{Re} \tag{4}$$

$$\frac{\partial \theta}{\partial \tau}+\frac{\partial U\theta}{\partial X}+\frac{\partial V\theta}{\partial Y}+\frac{\partial W\theta}{\partial Z}=\frac{\nabla^2 \theta}{Re\cdot Pr}. \tag{5}$$

In the above equations, the velocity has been nondimensionalized with the average incoming velocity U_{av} at the channel inlet, all lengths have been nondimensionalized with the channel height H, the pressure with ρU_{av}^2 and the nondimensional temperature is defined as $\theta = (T-T_\infty)/(T_w-T_\infty)$. Boundary conditions of interest in this investigation are:

top and bottom surfaces

$$u = v = w = 0; \quad T = T_w$$

for sidewall ($z = B/2$) and midplane ($z = 0$)

$$w = (\partial v/\partial z) = (\partial u/\partial z) = (\partial T/\partial z) = (\partial T/\partial z) = 0$$

at the entrance to the channel

$$u = u(y), \quad v = w = 0, \quad T = T_\infty.$$

At the exit of the channel, the continuative boundary condition is used by setting

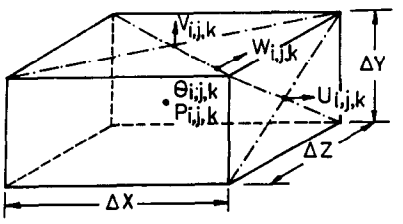

FIG. 4(a). Three-dimensional staggered grid showing the locations of the discretized variables.

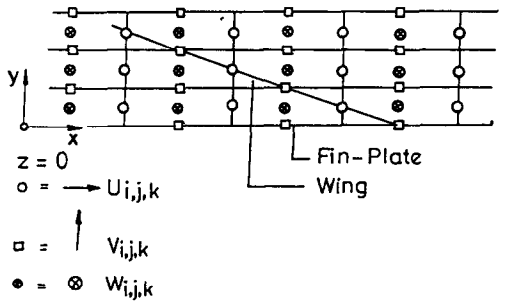

FIG. 4(b). Relative location of velocity components and wing on the x–y plane at $Z = 0$.

$$\frac{\partial^2 u}{\partial x^2} = \frac{\partial^2 v}{\partial x^2} = \frac{\partial^2 w}{\partial x^2} = \frac{\partial^2 T}{\partial x^2} = 0.$$

This ensures smooth transition through the outlet. It may be mentioned that by setting the second derivatives of the dependent variables in the flow direction equal to zero, we are not ignoring spacewise acceleration of the dependent variables, hence the aforementioned continuative boundary condition can be comfortably applied at the exit plane of a developing flow.

No-slip boundary conditions for the velocities on the obstacle are used. The temperature of the wing is constant and equal to T_w. The computational domain is divided into a set of cartesian cells. Staggered grid arrangements are used in which velocity components are defined at the cell faces to which they are normal (Fig. 4(a)). The pressure and temperature are defined at the centre of the cell. In order to state further details about the kinematic conditions on the wing, specific discussion can be made with the help of Fig. 4(b). The axial and normal components of velocity which fall directly on the wing are set to zero. Spanwise components do not fall directly on the wing. These W-velocities are interpolated on the wing from neighbouring cells and then the interpolated velocity components are set equal to zero. In order to take care of the punched holes beneath the wings periodic boundary conditions are used. It is assumed that the heat exchanger cores have a number of plates and on each plate the wing generators are punched out in such a way that the holes are perfectly aligned. Now, in our computational domain, part of the top and bottom boundaries must be set to identify the punched holes. For this purpose spacewise-periodic boundary conditions on the location of the punched holes have to be applied in the y direction. Here the period length is equal to the channel height H (Fig. 4(c)). The boundary conditions for the fictitious cells on the bottom are

$$u_{i,1,k} = u_{i,JRE,k}$$

$$v_{i,1,k} = 0.5\,(v_{i,JRE,k} + v_{i,1,k})$$

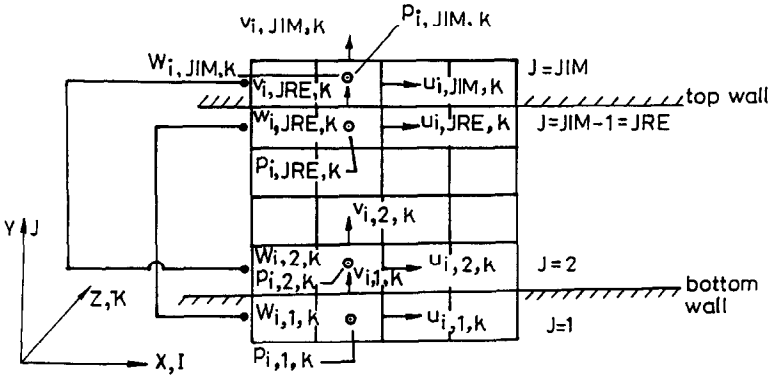

FIG. 4(c). Periodic boundary conditions for pressure and velocities on the top and the bottom wall.

$$w_{i,J,k} = w_{i,\mathrm{JRE},k}$$

$$p_{i,J,k} = p_{i,\mathrm{JRE},k}$$

(for all i,k in the punched holes)

and on the top

$$u_{i,\mathrm{JIM},k} = u_{i,2,k}$$

$$v_{i,\mathrm{JIM},k} = v_{i,2,k}$$

$$v_{i,\mathrm{JRE},k} = 0.5\,(v_{i,J,k} + v_{i,\mathrm{JRE},k})$$

$$w_{i,\mathrm{JIM},k} = w_{i,2,k}$$

$$p_{i,\mathrm{JIM},k} = p_{i,2,k}$$

(for all i, k in the punched holes).

Such boundary conditions have also been discussed by Hirt *et al.* [7].

METHOD OF SOLUTION

A modified version of the Marker and Cell (MAC) method [8, 9] is used to obtain the numerical solution of equations (1)–(5). Details of the solution procedure were discussed in the earlier investigation [6]. A concise description of the solution procedure is recorded herein for a ready reference. The solutions for the velocities are obtained in two parts. First, the velocity components are advanced explicitly using the previous state of flow having calculated viscous stresses and pressure gradients through a time step of duration $\delta\tau$. These explicitly advanced velocity components may not necessarily lead to a flow field with zero mass divergence in each cell. In the subsequent second part, correction of velocity is done through the simultaneous adjustment of pressure and velocity components in each cell by an iterative procedure. This iterative correction of the velocity field is continued until the mass conservation is ensured in each cell. This pressure–velocity iteration, through the implicit continuity equation, is equivalent to the solution of the Poisson equation for pressure [10]. The convective terms of equations (2), (3) and (4) are discretized by a hybrid scheme. The hybrid scheme combines upwind and central differencing of the convective terms to achieve the stability of the upwind method and the better formal accuracy of central differencing [11].

The solution procedure avoids the need for pressure boundary conditions as associated with the solution of the Poisson equation for pressure [12]. After evaluating the correct velocities, the energy equations are solved with an SOR technique to determine the temperature field.

Computational accuracy is calibrated by comparing peripheral average local Nusselt numbers predicted by our numerical scheme with those of available literature [13] for thermally developing and hydrodynamically developed flow through parallel plates. The results were found to be in agreement within about 5% for a Reynolds number of 500 and uniform wall temperature boundary conditions.

An effort was made to obtain grid-independent results. For $Re = 500$ and $Pr = 0.7$ in a channel ($\alpha = 2$) with a built-in delta wing ($\Lambda = 1$) at an angle of attack (β) of 26°, reasonable agreement between the results obtained for 15×26 and 20×30 cross-stream grids was found. In the foregoing specification of cross-stream grids, 15 and 20 refer to the number of grids in the y direction. Similarly, 26 and 30 refer to the number of grids in the z direction. However, for a 15×26 cross-stream grid in the y–z plane, 60 grid nodes were taken in the x direction for a nondimensional axial distance of 8.4. Grid independence was also tested for other geometrical and flow parameters. In each case, beyond a small value ($\pm 4\%$) further refinements of the grid size were not computationally economical.

Solutions are independent of the chosen domain in the x direction. This is the beauty of the continuative boundary condition ($\partial u^2/\partial x^2 = \partial v^2/\partial x^2 = \partial w^2/\partial x^2 = \partial T^2/\partial x^2 = 0$). At the outlet the second derivatives of the dependent variables in the x direction are set equal to zero. The continuative boundary condition can be applied at the outlet section of a developing flow. This condition does not impose any severe restrictions on the accelerating flow and has the least upstream influence. Smooth transition of flow through the exit boundary is indeed ensured by imposing such a condition.

The computations have been performed on an Apollo Domain 3500 workstation.

RESULTS AND DISCUSSION

A large number of computations have been performed at different Reynolds numbers and angles of attack (β) with a delta wing as a wing generator. Figure 5 shows a typical picture of the generation of vortices and their gradual deformation as they move downstream in the channel.

Figures 6(a) and (b) compare the velocity vectors on a longitudinal section (x–y plane) for $Re = 500$ and $Pr = 0.7$ for the cases with and without stamping on the channel walls respectively. The views are taken about the midplane of the channel. For the case with stamping, fluid gets entrained through the upper hole and there is loss of fluid through the hole underneath the wing. However, a spiralling structure of the main flow is discerned behind the wing for both cases. It is seen that, downstream, the magnitudes of the velocity vectors for the case with punched holes are less than those for the case without any stamping. This observation is made through the comparison of velocity vectors at the same axial location in both cases.

Comparison of cross-stream velocity vectors at a nondimensional distance of $X = 1.169$ from the inlet of the channel for the cases with and without stamping on the solid walls is obtained in Figs. 7(a) and (b). Due to the stamping on the walls a velocity field normal

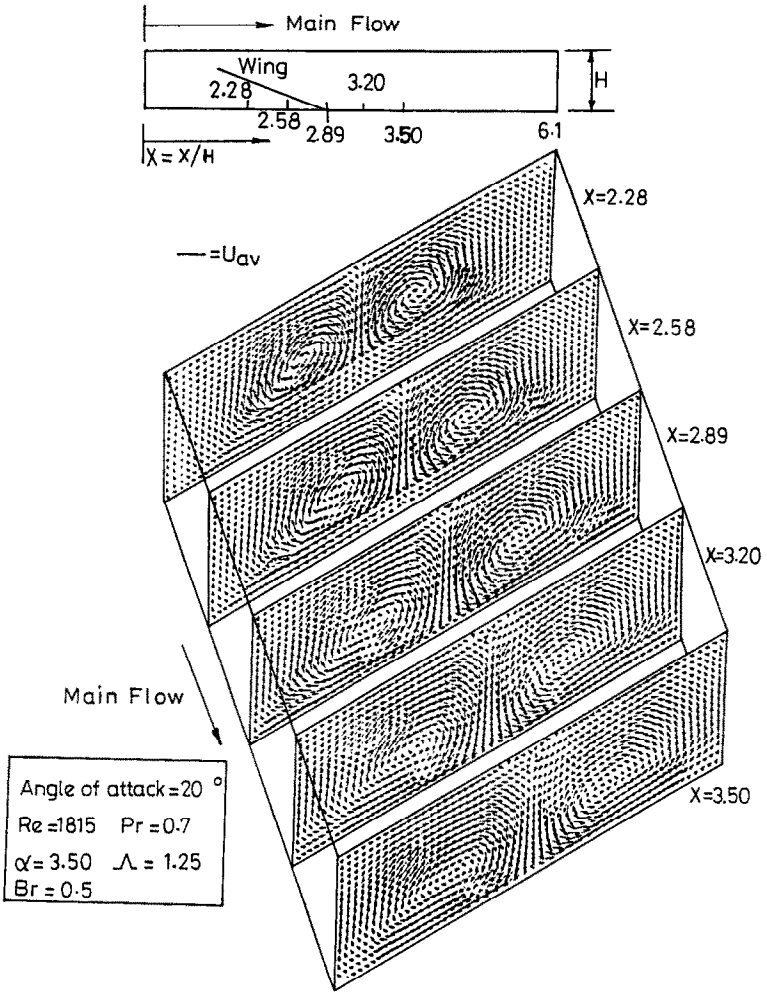

FIG. 5. Generation and deformation of the vortices in the channel.

to the vortical motion is induced in the downward direction. This induced downward normal velocity field reduces the strength of the vortical flow and, as compared with the case where there is no stamping, a decayed circulatory flow pattern is observed at the same axial location.

Before analysing the heat transfer results we can concentrate on understanding the basic mechanisms of heat transfer augmentation due to embedded longitudinal vortices. Figures 8(a) and (b) show the isotherms over two cross-planes located at two different axial locations in the channel. It is seen that as the fluid stream moves from an axial distance $X = 2.9$ to 3.538 the value of the isotherm at the core increases, whereas the value of the isotherm at the surface decreases. This can be attributed to the vortical nature of the flow field. These two plots imply that due to the better mixing of the cooler steam of the core with the hot fluid from the wall, the core temperature rises and at the same time heat is transferred through a relatively higher temperature gradient at the solid wall.

However, the heat transfer and the skin friction coefficients—the major performance parameters—are dependent on the Reynolds number and the geometrical parameters of the wing. In the following sections we shall discuss the influence of these governing parameters on the performance of the vortex generators. Air has been assumed as working fluid; hence the Prandtl number of this study has been fixed at a constant value of 0.7.

In order to have a quantitative distinction of the heat transfer performance the combined spanwise average Nusselt number

$$\overline{Nu}_{sa} = \frac{B(q_1+q_2)}{2\int_0^{B/2}(T_{w1}(x,z)-T_b(x))\,dz + 2\int_0^{B/2}(T_{w2}(x,z)-T_b(x))\,dz} \cdot \frac{H}{k} \quad (6)$$

has been calculated at each longitudinal location to depict heat transfer at any axial position in the chan-

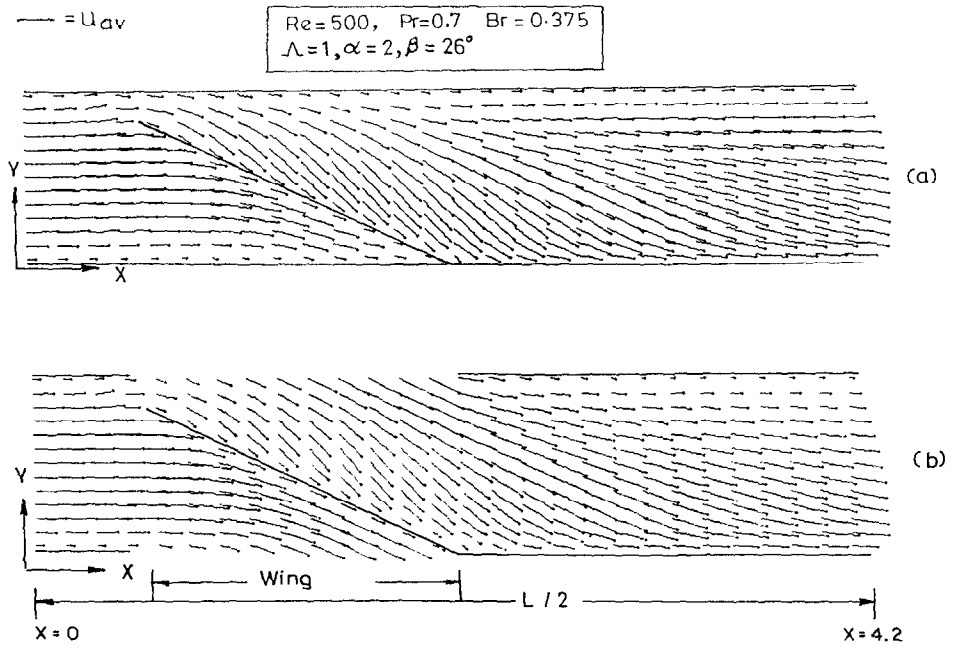

FIG. 6. Longitudinal velocity vectors at the midplane ($Z = 0$) of the duct. (a) Delta wing. (b) Delta wing with stamping.

nel. Figure 9 shows the longitudinal distribution of the combined spanwise average Nusselt number in the channel. In the region of the wing (from $X = 0.78$ to 2.36), the combined spanwise average Nusselt number rises to a high value up to a region behind the middle of the wing and then takes a plunge. A small dead water zone exists in the immediate neighbourhood behind the wing–body junction which eventually causes poor heat transfer at that location. Here, we are referring to the case with the built-in delta wing in the absence of any stamping. However, in the downstream of the wing, heat transfer is increased remarkably as compared with the plane channel without any obstruction. As such, even for a very long channel ($X = 8.4$), the enhancement in heat transfer at the exit of the channel is more than 34%. Enhancement in heat transfer is not so pronounced when the effect of punched holes beneath the wings is taken into account. Due to the downward normal stream at the cross-plane (as shown in Fig. 7(b)), the strength of the longitudinal vortices is reduced to a great extent and a spiralling flow with relatively less vortex strength exists. Disruption of boundary layer growth is also observed here but the improvement of the heat transfer coefficient is relatively lower than that of the case without any punched holes. However, at the exit the improvement of heat transfer as compared with the plane channel is about 10%. This improvement is even better in all the axial locations behind the wing.

In order to examine the influence of angle of attack on heat transfer we observe Fig. 10. It is observed that the combined spanwise average Nusselt number increases with increasing angle of attack. Wings with higher angles of attack (until vortex breakdown does not take place) produce vortices with higher strength which results in better heat transfer. At a non-dimensional axial distance of 4 from the inlet, for an angle of attack of 20°, we observe an enhancement of 45.4% in combined spanwise average Nusselt number over the case of a channel without any obstacles. Now at the same location, for $\beta = 26°$, an improvement of 10.6% in $\overline{Nu}_{sa}$ over the case of the 20° angle of attack is obtained. However, at the same location, an improvement of 26.42% over the case of the 20° angle of attack is discerned for $\beta = 30°$.

The effect of Reynolds number on combined spanwise average Nusselt number is clearly evident from Fig. 11. A higher Reynolds number signifies a higher mass flow rate and as a consequence a higher heat removal rate is observed. At the exit of the channel ($X = 8.4$), $\overline{Nu}_{sa}$ for $Re = 1815$ is 98.38% larger than that for $Re = 500$.

In this study, the length of the channel is well below the thermal entry length. What we have illustrated here is the influence of wing parameters and Reynolds number on the enhancement of heat transfer in a developing flow. It may be mentioned that the fully developed Nusselt number (in our case $Nu = hH/k$) for a channel flow with uniform wall temperature boundary condition is 3.77.

Augmentation in heat transfer is obtained at the price of increasing pressure drop. As we have mentioned earlier, when wing-type vortex generators are used for enhancing heat transfer coefficients, the increase in pressure drop is relatively less. In order to show the aforementioned performance of wing-type

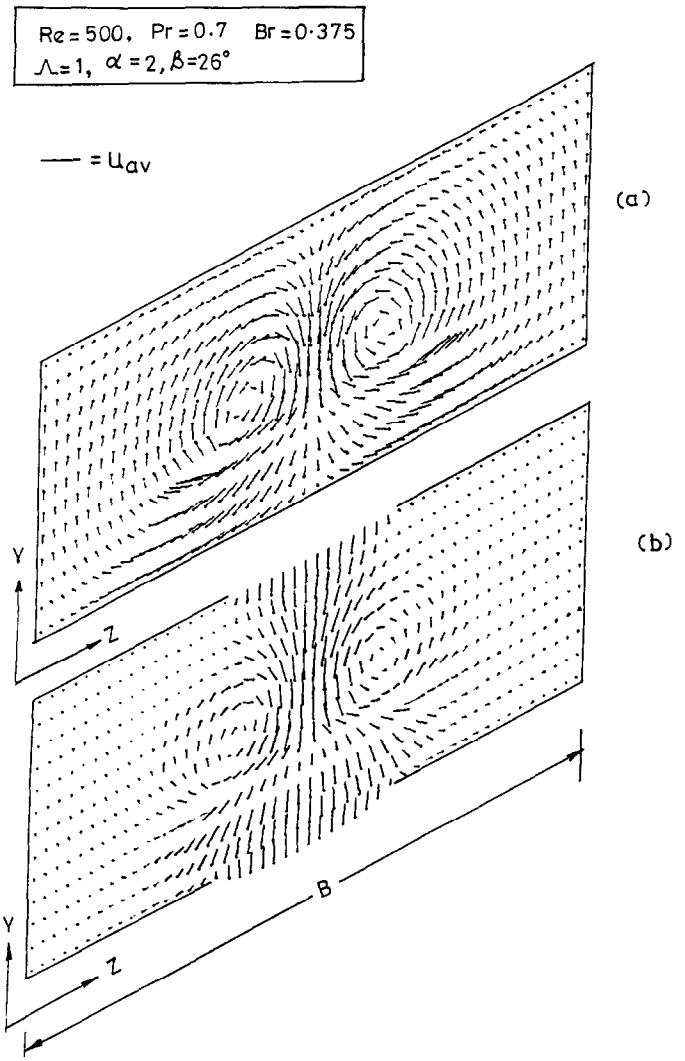

FIG. 7. Cross-stream velocity vectors at a nondimensional distance $X = 1.69$. (a) Delta wing. (b) Delta wing with stamping.

vortex generators, the combined spanwise average friction factor has been defined as

$$\bar{f} = \frac{\mu}{\frac{\rho}{2}U_{av}^2} \cdot \frac{\left[2\int_0^{B/2}\left(\frac{\partial u}{\partial y}\right)_{y=0} dz + 2\int_0^{B/2}\left(\frac{\partial u}{\partial y}\right)_{y=H} dz\right]}{2B}. \quad (7)$$

Figure 12 shows the distribution of combined spanwise average friction factor ($\bar{f} \times Re$) in the channel for three different cases. This parameter is not to be confused with Darcy's friction coefficient, rather it should be called Fanning's friction factor. As such this plot clearly shows the effect of stamping on the distribution of the combined spanwise average friction factor. As mentioned earlier, due to the stamped holes a downward normal stream is induced near the wing which reduces the strength of the longitudinal vortices generated by the delta wing. As a base case, for comparison, the combined spanwise average friction factor ($\bar{f} \times Re$) in the channel in the absence of any obstruction and stamping has been plotted. We have taken thermally developing and hydrodynamically developed flow. As expected, the ($\bar{f} \times Re$) value remains unchanged throughout in the channel for the flow without any obstacle and stamping. As such this value for a fully developed channel flow is 24 (see Shah and London [13]), but there the characteristic length in the definition of the Reynolds number is the hydraulic diameter, which is twice our characteristic length (H). However, with our definition, we obtain a ($\bar{f} \times Re$) value of 12 which is also a check for the computational accuracy. For a very long channel ($X = 8.4$) at the exit, the increase in ($\bar{f} \times Re$) in the channel for the case with a built-in wing generator (without stamping) over the ($\bar{f} \times Re$) value for a plane channel is 79%, whereas this value of friction factor

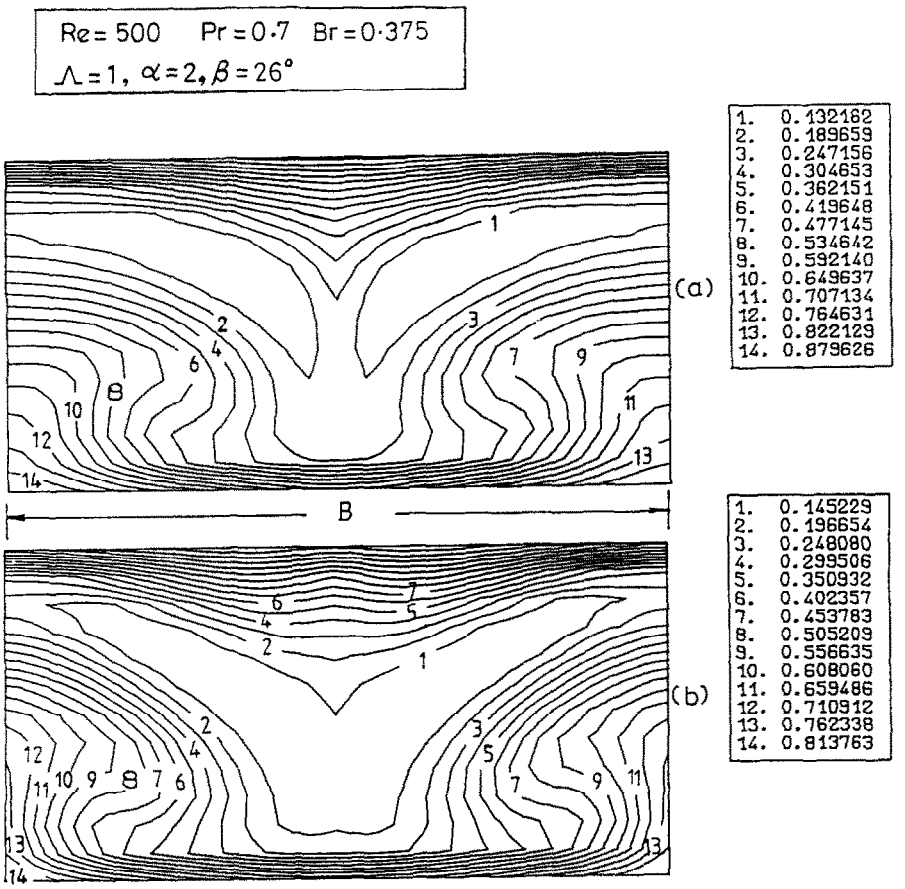

FIG. 8. Isotherms at cross-sections $X = 2.9$ (a) and $X = 3.538$ (b) from the inlet. The base of the wing is located at a distance $X = 2.36$ from the inlet.

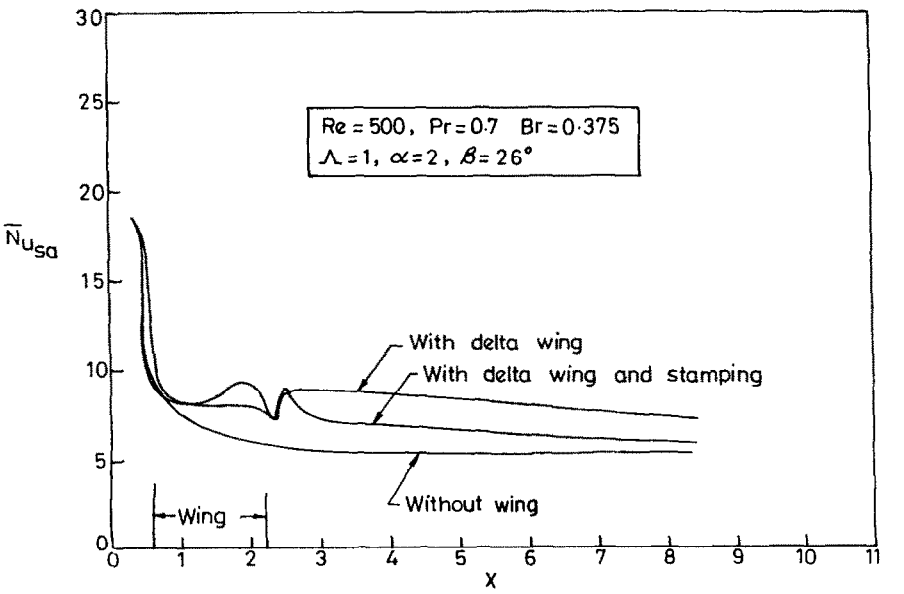

FIG. 9. Effect of stamping on the distribution of the combined spanwise average Nusselt number in the channel.

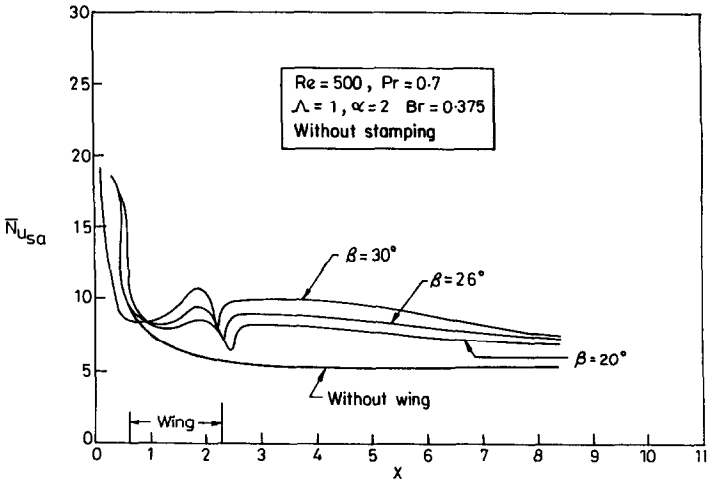

FIG. 10. Effect of angle of attack on the distribution of the combined spanwise average Nusselt number in the channel.

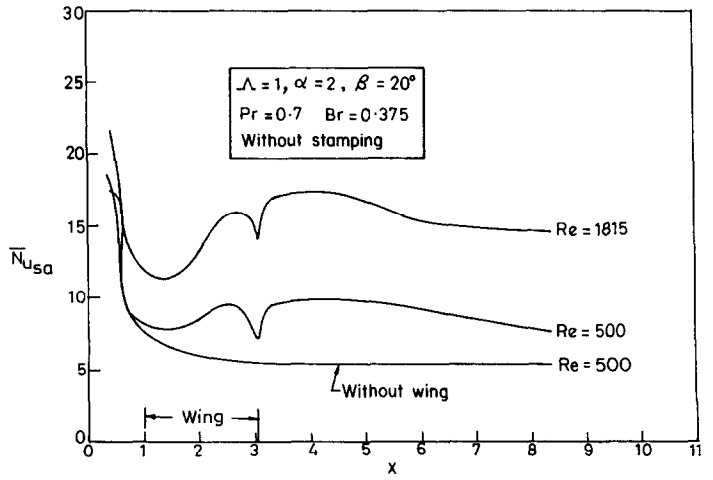

FIG. 11. Effect of Reynolds number on the distribution of the combined spanwise average Nusselt number in the channel.

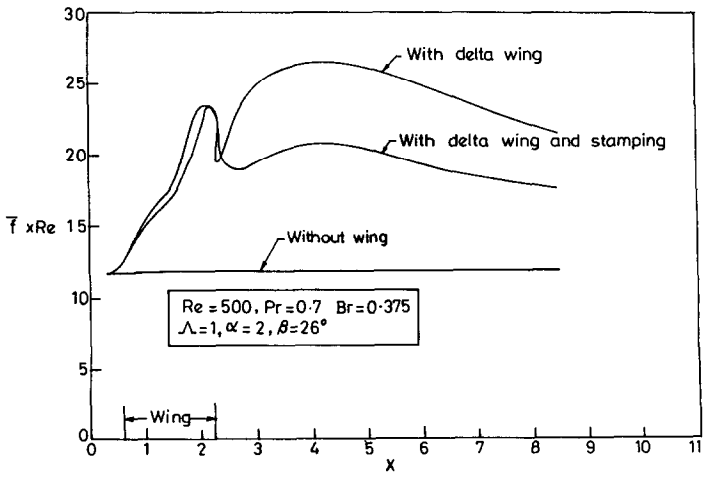

FIG. 12. Effect of stamping on the distribution of the combined spanwise average friction factor in the channel.

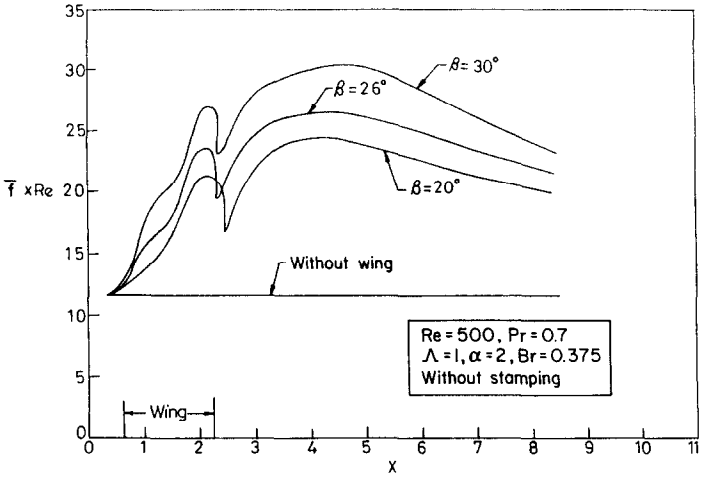

FIG. 13. Effect of angle of attack on the distribution of the combined spanwise average friction factor in the channel.

($\bar{f} \times Re$) is only 48% more than the plane channel value when the punched hole under the wing is taken into account.

Figure 13 shows the effect of varying the vortex generator's angle of attack while keeping the size constant. Increasing the angle of attack has the effect of increasing the vortex circulation which increases resistance and a higher value of combined spanwise average friction factor is obtained. Of course, this is associated with a higher heat transfer rate, as was depicted in Fig. 10. However, at the exit of the channel, ($\bar{f} \times Re$) for $\beta = 30°$ is 15% more than that for $\beta = 20°$ and ($\bar{f} \times Re$) for $\beta = 26°$ is 8.4% more than for $\beta = 20°$.

Figure 14 shows the effect of Reynolds number on ($\bar{f} \times Re$) while keeping the channel and the parameters related to the vortex generator constant. At the exit of the channel ($X = 8.4$), ($\bar{f} \times Re$) for $Re = 1815$ is about 83.18% greater than that for $Re = 500$. A higher mass flow rate increases the strength of the vortices which finally results in a higher drop in skin friction.

The model validation was performed through comparison with some published experimental results. Local Nusselt numbers along the centreline of the bottom plate with a delta wing at an angle of attack of 20° were calculated. Reynolds and Prandtl numbers for this computation are 1815 and 0.7, respectively. Here, local Nusselt number values were evaluated on the basis of entry temperature of the incoming fluid stream as

$$Nu_{xc} = \frac{-k\left[\left(\frac{\partial T}{\partial y}\right)_{y=0,z=0}\right]_x}{[T_w(x) - T_\infty]_{y=0,z=0}} \cdot \frac{H}{k}. \tag{8}$$

Figure 15 shows that the computed values of local Nusselt number compare favourably with the experimental results of Fiebig *et al.* [4]. In the experiment [4, 14], the channel walls had punched holes on them

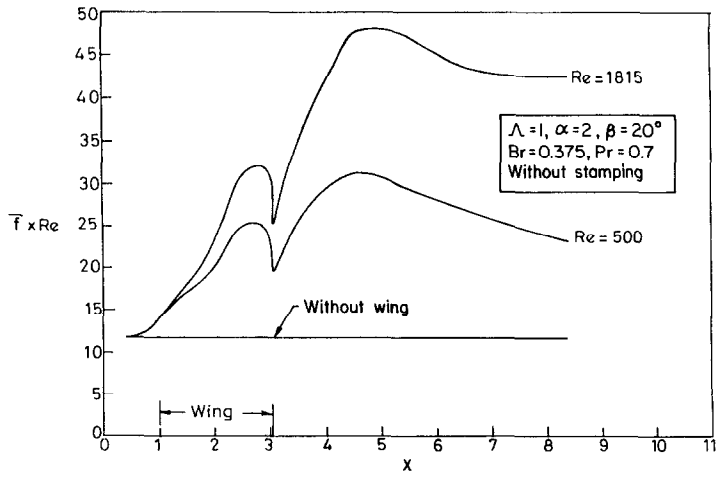

FIG. 14. Effect of Reynolds number on the distribution of the combined spanwise average friction factor in the channel.

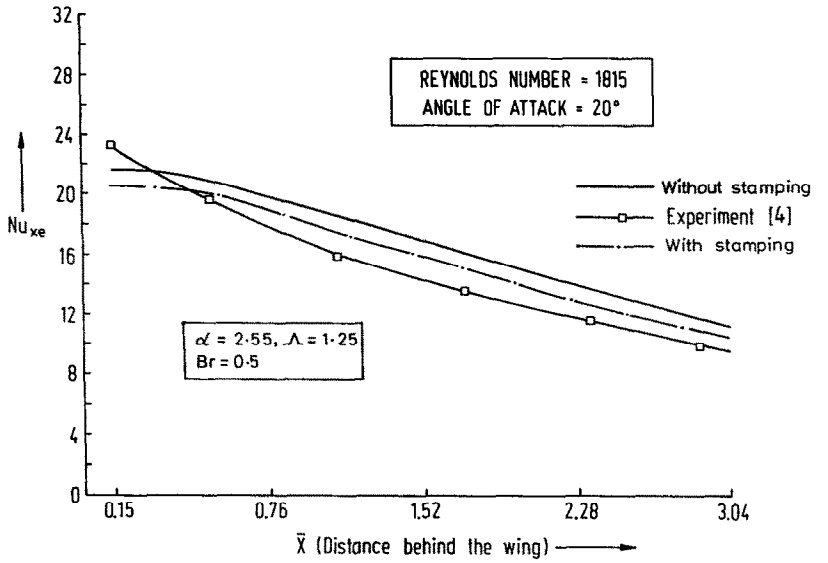

FIG. 15. Comparison of computed results with experimental observation.

and the experimental results are closer to the computed results for the case with stamping. The small discrepancy could be attributed to the physical boundary conditions on the channel wall. It was not possible to maintain perfect isothermal conditions on the plate surface during the experiments. As such the local heat transfer coefficients were determined by unsteady liquid crystal thermography. Measurement error is indeed minimal in this process; accuracy is within $\pm 4\%$. The intensity of turbulence was less than 2% in the experiments [4, 14] and its influence on the discrepancy of results can possibly be ignored.

Acknowledgements—We are grateful to the referees for valuable comments, and also to Prof. M. A. Faruqi of the Indian Institute of Technology, Kharagpur for providing us with an Apollo Domain 3500 workstation. This work was initiated by one of the authors (GB) during his stay as a postdoctoral fellow in the Federal Republic of Germany. A post-doctoral fellowship to the author (GB) from the Alexander von Humboldt Foundation is gratefully acknowledged.

REFERENCES

1. P. A. Eibeck and J. K. Eaton, Heat transfer of a longitudinal vortex embedded in a turbulent boundary layer, *J. Heat Transfer* **109**, 16–24 (1987).
2. F. J. Edwards and G. J. R. Alker, The improvement of forced convection surface heat transfer using surface protrusions in the form of (a) and (b) vortex generators, *Proc. Fifth Int. Heat Transfer Conf.*, Tokyo, Vol. 2, pp. 2244–2248 (1974).
3. C. M. B. Russel, T. V. Jones and G. H. Lee, Heat transfer enhancement using vortex generators, *Proc. Seventh Int. Heat Transfer Conf.*, Munich, Vol. 3, pp. 283–288 (1982).
4. M. Fiebig, P. Kallweit and N. K. Mitra, Wing-type vortex generators for heat transfer enhancement, *Proc. Eighth Int. Heat Transfer Conf.*, San Francisco, Vol. 6, pp. 2909–2913 (1986).
5. G. Biswas, N. K. Mitra and M. Fiebig, Computation of laminar mixed convection flow in a rectangular duct with wing-type built-in obstacles, AIAA Paper No. 88-2647, AIAA Thermophysics, Plasmadynamics and Lasers Conference, San Antonio (1988).
6. G. Biswas, N. K. Mitra and M. Fiebig, Computation of laminar mixed convection flow in a channel with wing-type built-in obstacles, *J. Thermophys. Heat Transfer (AIAA)* **3**, 447–453 (1989).
7. C. W. Hirt, B. D. Nichols and N. C. Romero, SOLA—A numerical solution algorithm for transient fluid flows, Los Alamos Scientific Lab. Report LA-5652 (1975).
8. F. H. Harlow and J. E. Welch, Numerical calculation of time-dependent viscous incompressible flow of fluid with free surface, *Physics Fluids* **8**, 2182–2188 (1965).
9. C. W. Hirt and J. L. Cook, Calculating three-dimensional flows around structures and over rough terrain, *J. Comput. Phys.* **10**, 324–340 (1972).
10. A. Brandt, J. E. Dendy and H. Ruppel, The multigrid method for semi-implicit hydrodynamic codes, *J. Comput. Phys.* **34**, 348–370 (1980).
11. Y. Jaluria and K. E. Torrance, *Computational Heat Transfer*, pp. 179–182. Hemisphere, New York (1986).
12. R. Peyret and T. D. Taylor, *Computational Methods for Fluid Flow*, Springer Series in Computational Physics, pp. 150–164. Springer, New York (1983).
13. R. K. Shah and A. L. London, *Laminar Flow Forced Convection in Ducts*, Advances in Heat Transfer Suppl. 1, pp. 169–176. Academic Press, New York (1978).
14. P. Kallweit, Längswirbelerzeuger für den Einsatz im Lamellenwärmetauschern, Doctoral Thesis, pp. 27–28, Inst. für Thermo- und Fluiddynamik, Ruhr Universität Bochum, F.R.G. (1986).

TRANSFERT THERMIQUE DANS UN CANAL AVEC DES GENERATEURS AILETES DE VORTEX

Résumé—On étend une étude précédente pour déterminer numériquement la structure de l'écoulement et les caractéristiques thermiques dans un canal rectangulaire avec une aile delta protubérante à la paroi inférieure. On obtient la solution numérique des équations complètes de Navier–Stokes et de l'énergie. On met en évidence l'augmentation du transfert thermique entre le fluide et les parois du canal. On détermine l'effet du générateur aileté de vortex sur le transfert thermique et le frottement pariétal ainsi que celui de l'angle d'attaque du générateur et du nombre de Reynolds. Le nombre de Nusselt moyen dans la largeur montre un accroissement allant jusqu'à 34 pour cent, même à la sortie d'un long canal pour un angle d'attaque de 26°.

WÄRMEÜBERGANG IN EINEM KANAL MIT EINGEBAUTEN FLÜGELÄHNLICHEN WIRBELERZEUGERN

Zusammenfassung—In Erweiterung einer früheren Arbeit wird in der vorliegenden Untersuchung die Struktur der Strömung sowie der Wärmeübergang in einem Rechteckkanal mit eingebauten Deltaflügeln untersucht, welche an der unteren Wand angebracht sind. Hierzu wird der vollständige Satz der Navier–Stokes-Gleichungen sowie der Energie-Gleichung numerisch gelöst. Dabei zeigt sich eine Verbesserung des Wärmeübergangs zwischen dem strömenden Fluid und der Kanalwand. Es wird der Einfluß eines unter den flügelartigen Wirbelerzeugern angebrachten Bohrlochs auf den Wärmeübergang und den Druckverlust bestimmt. Außerdem werden die Einflüsse des Anstellwinkels der Wirbelerzeuger und der Reynolds-Zahl untersucht. Die mittlere Nusselt-Zahl zeigt eine Zunahme um 34%, dies gilt bei einem Anstellwinkel von 26° sogar am Ende eines langen Kanals.

ТЕПЛОМАССОПЕРЕНОС В КАНАЛЕ С ВСТРОЕННЫМИ КРЫЛЬЧАТЫМИ ГЕНЕРАТОРАМИ ВИХРЕЙ

Аннотация—В работе дается численное определение структуры течения и характеристик теплообмена в прямоугольном канале со встроенным треугольным крылом, выступающим из нижней стенки. Проведено численное решение полных уравнений Навье–Стокса и энергии. Хорошо видно увеличение интенсивности теплообмена между потоком жидкости и стенкой канала. Определено влияние отверстия под крыльчатым генератором вихрей на характеристики теплопереноса и поверхностного трения, а также влияние угла атаки генеяатора вихрей и числа Рейнольдса на теплообмен и поверхностное трение. Значение сложного осредненного по размаху крыла числа Нуссельта возрастает на 34% на выходе из длинного канала при угле атаки 26°.